Available online at www.sciencedirect.com
ScienceDirect
Journal of Magnetic Resonance 190 (2008) 280–291
JMR Journal of Magnetic Resonance
www.elsevier.com/locate/jmr

Cryogenic Q-band (35 GHz) probehead featuring large excitation microwave fields for pulse and continuous wave electron paramagnetic resonance spectroscopy: Performance and applications

Jörg Forrer [a], Inés García-Rubio [a], Rolf Schuhmam [b], Rene Tschaggelar [a], Jeffrey Harmer [a,*]

[a] *Laboratorium für Physikalische Chemie, ETH Zürich, Zürich CH-8093, Switzerland*
[b] *Fachgebiet Theoretische Elektrotechnik, Universität Paderborn, 33098 Paderborn, Germany*

Received 17 July 2007; revised 11 October 2007
Available online 17 November 2007

Abstract

The construction and performance of a Q-band (35 GHz) cryogenic probehead for pulse electron paramagnetic resonance and continuous wave electron paramagnetic resonance measurements with down-scaled loop gap resonators (LGRs) is presented. The advantage of the LGR in comparison to TE_{012} resonators lies in the large B_1 microwave (mw) fields that can be generated with moderate input mw power. We demonstrated with several examples that this allows optimal performance for double-quantum electron coherence, HYSCORE, and hyperfine decoupling experiments employing matched and high turning angle mw pulses with high B_1-fields. It is also demonstrated that with very low excitation power (i.e. 10–40 mW), B_1-fields in LGRs are still sufficient to allow short mw pulses and thus experiments such as HYSCORE with high-spin systems to be performed with good sensitivity. A sensitivity factor Λ_{rs} of LGRs with different diameters and lengths is introduced in order to compare the sensitivity of different resonant structures. The electromagnetic field distribution, the B_1-field homogeneity, the E_1-field strength, and the microwave coupling between wave guide and LGRs are investigated by electromagnetic field calculations. The advantage and application range using LGRs for small sample diameters is discussed.

Keywords: EPR; Loop gap resonator; DQ EPR; HYSCORE; Hyperfine decoupling; Q-band probehead

1. Introduction

Pulse electron paramagnetic resonance (EPR) spectroscopy at frequencies around 35 GHz is of high importance because of the nuclear Zeeman spectral resolution, the reduced second-order effects, the suitability for electron spin echo envelope modulation (ESEEM) spectroscopy, the g value resolution, and the orientation selectivity of the microwave (mw) pulses [1–4]. Since EPR was discovered a considerable amount of information about the design of various probeheads has been reported [5–7] and a large number of patents have been filed. Nevertheless, probehead design remains a critical factor and thus attracts the attention of EPR engineers and spectroscopists. Sensitivity, filling factor, adjustable bandwidth, and optimum pulse power efficiency are the important adjustable trade-off parameters in pulse EPR applications.

In our laboratory the three most successfully applied resonators in pulse EPR have been: the bridged loop gap resonator (BLGR) which has been used in a large number of novel experiments [8–13] because of its thermal stability, transparency to rapid B_0-field steps and to radio frequency (rf) radiation, the latter making it suitable for electron nuclear double resonance (ENDOR) techniques [14–19]; the loop gap resonator (LGR) [20–23] because of its mechanical stability and ease of construction; and the dielectric resonator (DR) [24,25] which consists of a sap-

* Corresponding author.
E-mail address: harmer@phys.chem.ethz.ch (J. Harmer).

1090-7807/$ - see front matter © 2007 Elsevier Inc. All rights reserved.
doi:10.1016/j.jmr.2007.11.009

phire ring with a dielectric constant of about 10, attractive because of its nonmetallic structure, easy optical access, minimal mw losses, wide mw coupling range, and its excellence for ENDOR applications. Both the BLGR and the LGR have high B_1-field homogeneity along the sample main axis [8,26–28,32]. All three resonant structures are distinguished by a high filling factor, good mw coupling possibilities, and a high pulse power efficiency $\Lambda_p = B_1/\sqrt{P_{mw}}$, where B_1 is the mw magnetic field in the sample volume and P_{mw} is the incident mw pulse power. All three resonators described above are suitable for performing two-dimensional EPR experiments. With the BLGR and the DR, experiments using rf fields and field modulations and jumps, such as ENDOR, nuclear-Zeeman resolved ESEEM (NZ-ESEEM) [12], electron-Zeeman resolved EPR (EZ-EPR) [29], anisotropic resolved EPR (AR-EPR) [30], and longitudinal detection EPR [31], are performed with high sensitivity.

We have recently demonstrated [32] that pulse power efficiency Λ_p improvements are achieved with small diameter and short length LGRs (i.e. small sample volume) and that Λ_p for pulse EPR performance at 35 GHz is excellent. Our first successful pulse EPR experiments in this laboratory [33–35] have been performed at 9.5 GHz with a *three-loop-two-gap* 7 mm long LGR [22]. The *three-loop-two-gap* resonators described in the present work are in a way a down-scaled version of the resonators in [22]. They are constructed out of copper for pulse EPR measurements and for continuous wave (CW) EPR measurements out of machineable ceramic (MACOR) that is silver plated. Among the features of the 35 GHz LGR are the high pulse power efficiency Λ_p, the magnetic field homogeneity in the

Table 1
Dimensions of the *three-loop-two-gap* LGRs (rows *A* and *B*) and of the *two-loop-one-gap* LGRs (rows *C* and *D*)

D-LGR	d_0[a] (mm)	d_1[b] (mm)	h[c] (mm)	l[d] (mm)	w[e] (mm)	d[f] (mm)	f_0[g] (GHz)	f_0[h] (GHz)
A	2	2.28	3	0.3	0.61	1.6 × 1.0	36.8	34.2
B	1	2.28	3	0.764	0.27	0.9 × 0.7	35.3	34.5
C	0.45	2.3	3	1.05	0.19	0.4 × 0.3	35.6	35.2
D	0.45	2.0	0.25	1.05	0.126	0.4 × 0.3	35.5	35.1
TE_{102}[i]						1.6 × 1.0	35.5	35.2

The different quantities d_0, d_1, h, l, and w are defined in Fig. 2. The resonant frequencies are measured with a calibrated network analyzer (hp 8722 ES).
[a] Sample loop diameter.
[b] Coupling- (or side-) loop diameter.
[c] LGR height.
[d] Gap length.
[e] Gap width.
[f] Outer × inner quartz tube diameters.
[g] Resonance frequencies of empty LGRs and TE_{102} rectangular cavity resonator.
[h] Resonance frequencies with empty quartz tube.
[i] TE_{102} rectangular cavity resonator dimensions: 10.3 × 7 × 3.7 mm.

Table 2
Sensitivity factor $\Lambda_{rs} = ESE_{max}/V_{sample}$, S/N ratio, loaded quality factor Q_L and pulse power efficiency $\Lambda_p = B_1/\sqrt{P_{mw}}$ of the *three-loop-two-gap* LGRs (rows *A* and *B*1–3), the *two-loop-one-gap* LGRs (rows *C* and *D*) and of the TE_{102} rectangular cavity resonator

Resonator	Loop diameter d_0 (mm)	LGR high h (mm)	MW pulse power[a] P_{mw} (mW)	ESE amplitude (mV)	Sensitivity factor Λ_{rs}[d] (mV/mm^3)	S/N[b]	Q_L[c] (RT)	MW pulse efficiency Λ_p (mT/$\sqrt{W}$)
A	2	3	80	150	63	53	250	0.39
B.1	1	3	16	150	130	53	700	0.87
B.2	1	3	32	100	86	35	400	0.61
B.3	1	3	39	80	69	29	270	0.56
C	0.45	3	11	36	169	8.4	210	1.04
D	0.45	0.25	4	6	340	2	205	1.7
	Dimensions (mm)							
TE_{102}	10.3 × 7 × 3.7		630	60	11	21	270	0.14

[a] The incident mw pulse power P_{mw} is measured at constant receiver gain and bandwidth at maximum ESE amplitude using a ICF sample with the sequence $\pi/2$–τ–π–τ–echo ($t_{\pi/2} = 80$ ns, $t_\pi = 160$ ns, $\tau = 300$ ns). The generated B_1-field is approximately 0.11 mT. The LGRs as well as the TE_{102} rectangular cavity resonator coupling (scattering parameter, S11) was kept between −15 and −25 dB.
[b] The S/N is calculated from the screen shots of the ESE amplitudes and the following noise trace at room temperature.
[c] Q_L is the loaded quality factor measured with a calibrated network analyzer (hp 8722 ES) at a coupling S11 of −15 to −25 dB at room temperature (RT) with quartz tubes filled with ICF as shown in Table 1.
[d] Λ_{rs} is the resonator sensitivity factor. It defines the ratio between the maximum ESE amplitude and the sample volume given in Table 1 of an ICF sample. The ESE sequence was $\pi/2$–τ–π–τ–echo ($t_{\pi/2} = 80$ ns, $t_\pi = 160$ ns, $\tau = 300$ ns).

sample volume, and the large achievable bandwidth. The LGR is therefore suitable for pulse experiments where short intense mw pulses are required (e.g. ESEEM, hyperfine decoupling, and double-quantum (DQ) electron coherence experiments), for CW EPR experiments where the sample is not be saturated using high B_1-fields, and for Fourier transform EPR. The mw power saving operating with LGRs instead of conventional cylindrical TE_{011} [36] or rectangular TE_{102} cavity resonators is measured to be a factor of up to 150, depending on the LGR dimensions, see Tables 1 and 2.

2. Performance

2.1. Spectrometer

Pulse EPR measurements were preformed on our home-made Q-band (34–36 GHz) CW/pulse EPR spectrometer [1] that has been upgraded with a home-made eight channel pulse forming unit and a home-made CW and pulse mw bridge with a mechanically and electrically controllable 50 mW Gunn oscillator that can be locked with an automatic frequency control circuit (AFC) to the LGR or cavity resonator. Data acquisition and manipulation, pulse programming and timing, the B_0-field control, the CW modulation unit, the CW receiver and the DICE ENDOR unit are all maintained by a Bruker ELEXSYS E580 console. High power mw pulses are generated at 35 GHz by a 100 W traveling wave tube (TWT) amplifier (Applied System Engineering, model 187 Ka). As a proof of concept also a 100 mW amplifier (MITEQ, model AMF-6F-2000-4000-90-20P) with a noise protection switch (General Microwave, model F9014) was used (instead of the 100 W TWT amplifier) as described in the application part. This demonstrates that a low power source produces sufficient excitation fields in the LGR for experiments with i.e. high-spin systems. For low temperature work at 5 K an Oxford CF 935 cooling system is used. CW and pulse signal detection is achieved with 35 GHz down conversion (bandwidth DC to 1 GHz).

2.2. Cryogenic probehead design

A probehead was constructed for several LGRs designed for 1.6, 0.9, and 0.4 mm o.d. quartz tubes (resonators *A*, *B*, *C*, and *D* in Tables 1 and 2) and allows easy sample exchange at temperatures from 5 to 300 K. The probehead construction is shown in Fig. 1. The lower part shown in Fig. 1b consists of the LGR housing (copper or MACOR block) (see also Fig. 2), coupled via the iris-coupler plate (number 17 in Fig. 1) to the WR28 wave guide (4). Both the LGR housing (16) and the iris-coupler plate have the outside dimensions of the WR28 flange. The iris coupler is remotely tunable (see below). The lower WR28 wave guide section and the cast H-bend (MDL, type 28BH22B) that connects to the iris-coupler plate are made from copper. The exchangeable sample tube holder with an

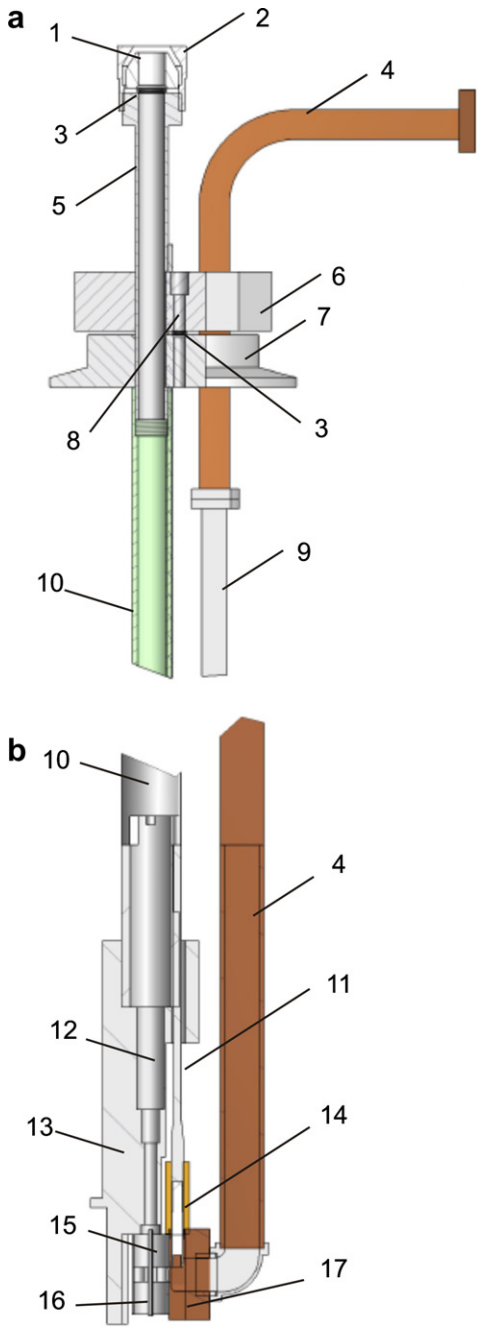

Fig. 1. (a) Upper and (b) lower cross-section part of the cryogenic probe head. (1) Teflon plunger, (2) cover nut, (3) O-ring, (4) WR28 Cu wave guide, (5) stainless steel (st. st.) sample access tube extension, (6) Al-flange, (7) st. st. flange, (8) vacuum feed through, (9) WR28 st. st. wave guide, (10) epoxi sample access tube, (11) st. st. rod for remote tuning control, (12) sample clamp E600-1022/9 (Bruker), (13) PEEK intersection, (14) PEEK tuning rod, (15) sample tube, (16) interchangeable LGR, and (17) Cu iris-coupler plate.

o.d. of 8 mm (not shown) (Bruker ER 4118SR sample rod, with a E600-1022/9 sample clamp on top) is guided through the 12×8 mm i.d. epoxy sample access tube (10) via a Polyetheretherketon (PEEK) [37] intersection (13) to the MACOR block (Fig. 2a). This intersection centers the quartz sample tube precisely in the sample loop (d_0) of the LGR, allows sample exchange at all temperatures,

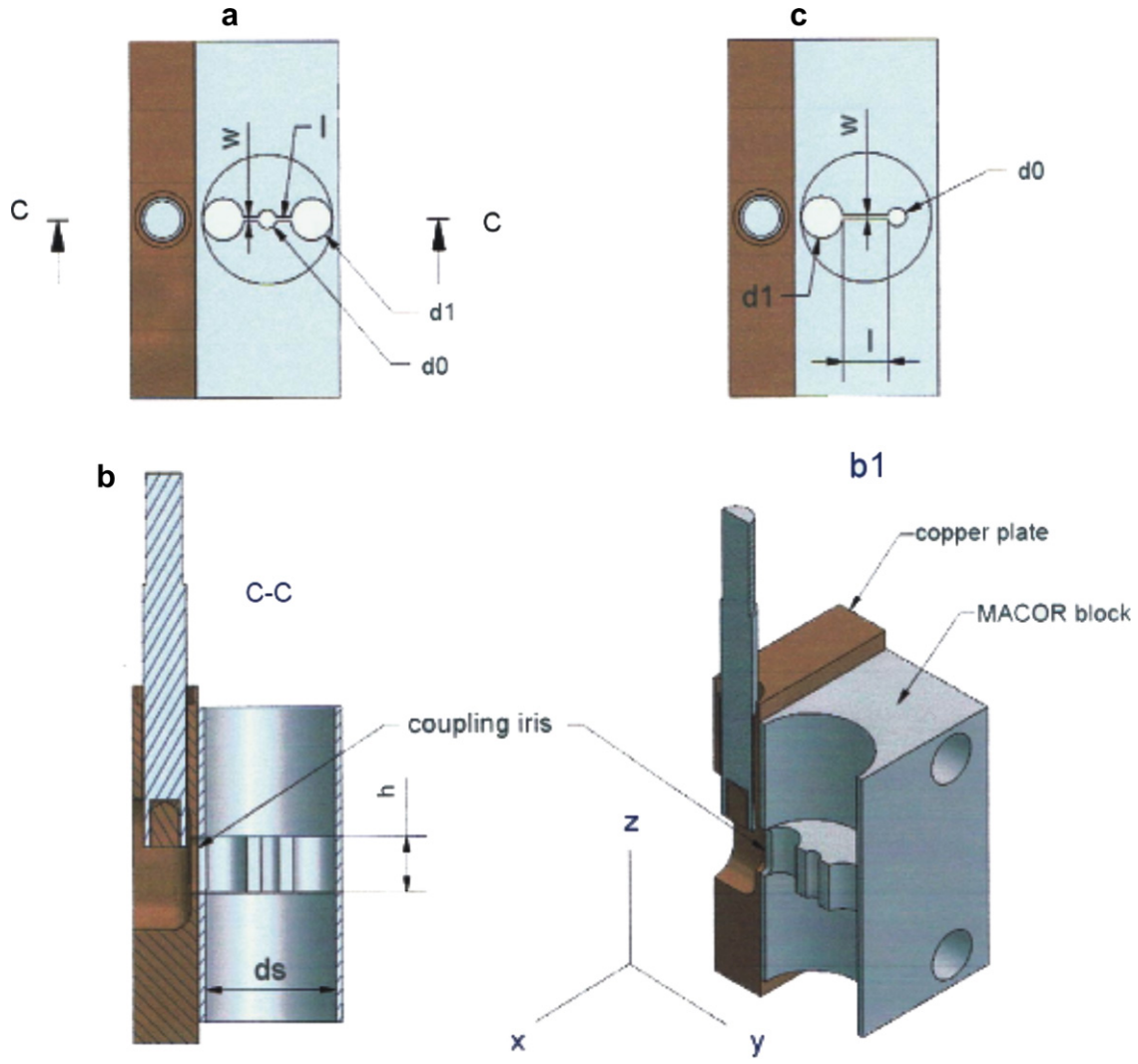

Fig. 2. *x–y* cross-section (a) of the *three-loop-two-gap* (c) of the *two-loop-one-gap* LGR with the copper iris-coupler plate and *y–z* cross-section at the cut "c-c" (b and b1) with the copper iris-coupler plate, PEEK tuning rod with copper tip and coupling iris.

connects the sample access tube to the LGR housing and adds additional mechanical stability. It serves also to fix the 100 kHz B_0-field modulation Helmholtz coil (not visible) used in CW-EPR, NZ-ESEEM [12], EZ-EPR [29], and AR-EPR [30], experiments which are ideally implemented with the small size (down-scaled) 35 GHz LGRs.

The upper part of the probehead shown in Fig. 1a consists of an upper Al-flange (6) and a lower stainless steel (st. st.) flange (7) that connects to an Oxford cryostat via an O-ring carrier plate. The two plates clamp the O-rings (3) of the vacuum feed troughs (8) for the thermocouple wires, the B_0-modulation wire pairs, and the drive shaft for remote tuning control of the mw coupler tuning rod (14). The copper WR28 wave guide (4) and st. st. sample access tube extension (5) are hard soldered onto the lower st. st. flange. Two BNC plugs (not visible) for the B_0-modulation coil drive input and the thermocouple output are attached on the upper Al-flange. A further O-ring (3) held by the Teflon plunger (1) in the cover nut (2) is clamped between the sample tube holder and the top of the st. st. sample access tube extension.

The wave guide He gasket (not visible) is clamped between the upper two WR28 flanges and consists of a 20 μm thick Mylar foil. The wave guide section connecting the lower and upper parts (9), shown in Fig. 1a, is made of stainless steel that is silver covered inside [38].

2.3. LGR dimensions and parameters

The LGR structure [20,28,21,39] is shown in Fig. 2. The holes with i.d. d_s are for the sample access ($d_s = 7$ mm for resonator *A* and *B* and 4.5 mm for resonator *C* and *D*), and serve to reduce mw radiation. In between the two holes is the disc with height *h* where the LGR structure is cut in. The two large outside loops with inner diameter (i.d.) d_1 are connected to the small center sample loop with i.d. d_0 by two equal gaps of length *l* and width *w*. The resonant frequency is mainly adjusted by the dimensions *w* and *l* for a

resonant frequency between 35 and 36 GHz. The holes and gaps are cut either by a water beam technique into the MACOR disc and then the structure is coated with 2–3 μm of pure Ag [38], or in the case of the copper disc by electro spark erosion. The spark erosion machine from AGIE (model "Challenge") used to cut the LGR structures, allows cuts with programmable surface qualities leading to different unloaded quality factors (Q) of the LGR.

Additional shielding is achieved by caps covering the holes with i.d. d_s at the top and at the bottom. Through the top cap the sample is guided to the sample hole. Through the hole in the bottom cap helium gas can flow to the sample.

Table 1 shows the dimensions and resonant frequencies of the two *three-loop-two-gap* LGRs (rows *A* and *B*) and the two *two-loop-one-gap* LGRs (rows *C* and *D*) [32,27]. The measured resonance frequency f_0^h depends also on the positioning and the symmetry of the quartz tube and may vary by up to ca. 50 MHz.

The sample hole diameters are designed to achieve the highest filling factors with the corresponding quartz tube diameters at the cost of a large resonant frequency shift between the empty and the quartz tube loaded resonators (see Table 1). The largest resonance frequency shift occurs with the 1.6×1.0 mm quartz tube in resonator *A*. The frequency shifts are caused by the quartz sample tubes entering areas of significant mw E_1-field strength. As shown in the field calculations of Fig. 3b and c, the quartz tube has the effect of *decreasing* the E_1-field strength in the sample area (compare the E_1-field distribution in the sample and side holes). To avoid the necessity of frequency tuning, the resonant frequency of all the LGRs and the TE_{102} cavity resonator (empty) are placed on the upper end of our tunable 2 GHz spectrometer frequency range.

Table 2 presents the electron spin echo (ESE) signal amplitudes, the sensitivity factor (Λ_{rs}), the S/N ratio, and the pulse efficiency (Λ_p) measured with the four different LGRs *A*, *B*, *C*, *D* and the rectangular TE_{102} cavity resonator. The LGRs *B*1–3 have the same dimensions (given in Table 1) but different surface qualities leading to different Q_L factors. The pulse efficiency factor $\Lambda_p = B_1/\sqrt{P_{mw}}$ gives information about the ratio of the pulse B_1-field strength and the square root of the incident mw pulse power. The incident mw pulse power P_{mw} is measured at the maximum ESE amplitude of γ-irradiated Ca formate (ICF), using the sequence $\pi/2$–τ–π–τ–echo ($t_{\pi/2} = 80$ ns, $t_\pi = 160$ ns, $\tau = 300$ ns), that generates a B_1-field of approximately 0.11 mT. Λ_p depends on the actual working conditions of the LGRs because the loaded quality factor Q_L differs for each mw coupling adjustment, for each new sample tube introduced and therefore also on the incident power that generates the maximum ESE amplitude. Experimental Q_L values have to be measured with the experimental conditions (temperature, sample, etc.) from the pulse response of the LGR [39].

The results in Table 2 show that, among the resonators with the same bandwidth (*A*, *B*.3, and *C*, Q_L around 250), LGR *A* generates the largest ESE amplitude with the best signal to noise ratio (S/N) but requires the largest sample tube (sample volume) and the largest incident mw power, which is typically a limiting factor. Comparing LGR *A* with the TE_{102} rectangular cavity resonator with the same bandwidth and sample volume, the later requires 8 times more power and achieves ca. half of the S/N ratio. The smallest sample tube (volume) in resonator *D* generates the smallest ESE amplitude with the lowest S/N but requires the lowest incident mw power (highest efficiency and sensitivity factor). The resonator sensitivity factor $\Lambda_{rs} = ESE_{max}/V_{sample}$ is introduced to compare the sensitivity of the different resonator structures and to obtain information about the achieved filling factor. The ESE amplitude is proportional to $\sqrt{Q_L}$, the filling factor, the sample volume and it also depends on the mw coupling. The maximum ESE amplitude, measured to determine Λ_p, is also used to determine Λ_{rs} for the particular sample dimensions shown in Table 1. The spin concentration of the samples and overall receiver gain and bandwidth was the same for all measurements. The low volume *two-loop-one-gap* LGRs *C* and *D* achieve the highest Λ_{rs} value, more than twice the value of the *three-loop-two-gap* LGR for similar Q_L values (resonators *A* and *B*.3). The lowest Λ_{rs} value was calculated for the TE_{102} cavity resonator. Despite the highest Λ_{rs} and Λ_p of the small resonators *C* and *D*, the S/N ratio is low due to the constant receiver noise level and the small echo amplitude observed. To obtain the S/N ratio achieved with resonator *B*.1, it takes for resonator *D* about a 600 times longer measurement time. The S/N ratio is determined at room temperature from a single ESE and the following noise trace recorded on an oscilloscope (bandwidth of 1 GHz).

For a particular application the available sample size and mw power dictate which resonator will lead to an optimum EPR signal or effect (i.e. ESEEM effect) [40].

2.4. Microwave coupling

The microwave iris coupler (number 17 in Fig. 1) between the LGR and the H-bend WR28 wave guide is a down sized version of the coupler structure used by Varian and later by Bruker. The mw coupler consists of a 3 mm thick Cu plate with WR28 flange dimensions with a $7 \times 3.0 \times 2.9$ mm round-shaped groove (see Fig. 2b–b1) that terminates the wave guide. The groove is opened by a 3×1.0 mm slot in the middle along the z-axis. The whole structure is positioned above the 3×0.8 mm iris of the LGR block. The coupling range is mainly given by the iris dimension. Insertion of interchangeable iris plates (thickness 0.1 mm) between the LGR housing block and the iris-coupler plate allows a further iris width reduction used for coupling LGRs with high Q_L values. It allows a step wise reduction of the iris width from 0.8 to 0.4 mm. Fine tuning is realized by the 1.5 mm diameter, 2 mm thick copper tip pressed into the top of a 2 mm diameter Teflon or high-strength polymer PEEK rod (Figs. 1b and 2b–b1). For lower Q_L values the Cu tip is moved toward the mid-

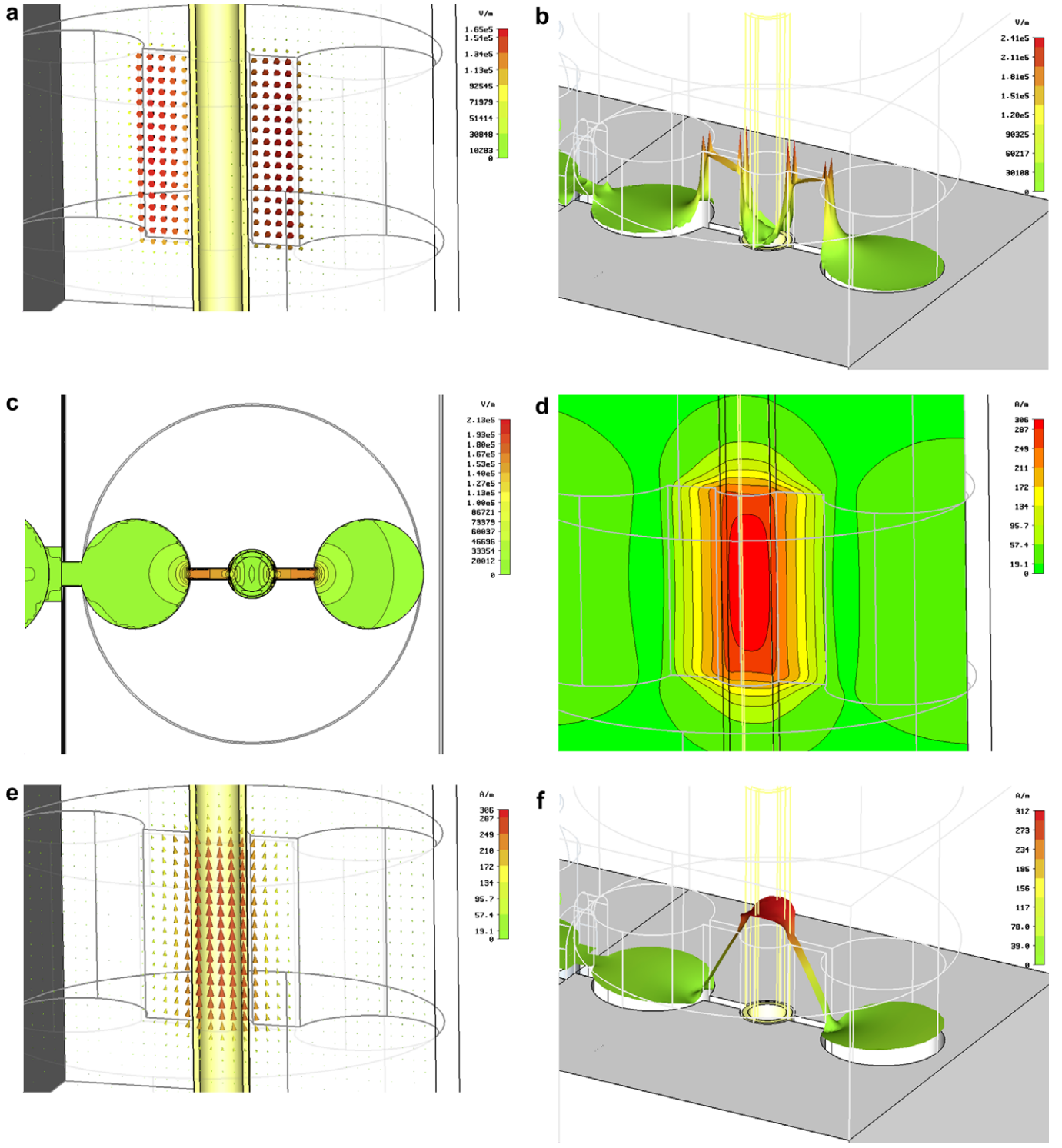

Fig. 3. (a) Vector representation of the E_1-field distribution in the y–z plane of the LGR type $B.1$. Cut through the middle of the quartz sample tube, gaps, and loops. (b) Three-dimensional representation of the E_1-field intensity distribution in the x–y plane at half high h (middle) of the LGR type $B.1$ with coupling iris and a 0.9×0.7 mm quartz sample tube. (c) E_1-field intensity in the x–y plane at half high h of the LGR type $B.1$ with coupling iris and a 0.9×0.7 mm quartz sample tube. The field change between the contour lines is 6%. (d) B_1-field intensity distribution in the z–y plane of the LGR type $B.1$ with a 0.9×0.7 mm quartz sample tube. The field change between the contour lines is 10%. (e) Vector representation of the uniform B_1-field distribution in the z–y plane of the LGR type $B.1$. Cut through the middle of the quartz sample tube, gaps, and loops. (f) Three-dimensional representation of the B_1-field intensity distribution in the x–y plane at half high h of the LGR type $B.1$ with coupling iris and a 0.9×0.7 mm quartz sample tube.

dle, for higher Q_L values it is pulled up above the iris in the round-shaped groove [41]. The influence of the Cu tip is sufficient for critically coupling but limited for overcoupling. Further tuning improvement is possible by sorely rotating or moving of the sample tube. The achieved coupling, (S11) is between −15 and −25 dB.

2.5. Electromagnetic field simulations

The use of a large sample size for low temperature measurements to improve the signal amplitude brings as a consequence larger resonant frequency shifts than in rectangular resonant cavities due to the higher electric field strengths in the quartz tube walls. Information about the electromagnetic field distribution is therefore of special interest.

For the electromagnetic field simulations in the 1 mm LGRs (*B*), we apply the commercial tool CST MICROWAVE STUDIO (MWS) [42]. The simulation method is the Finite Integration Technique (FIT) with the PBA-extension, which is able to accurately model curved interfaces within a Cartesian mesh. The complete structure including all coupling elements (iris, coupling screw and transition to waveguide) is modeled by roughly 600.000 mesh cells, leading to a mesh resolution in the most critical parts (gaps and probe area) below 40 μm, equivalent to 6 cells over the gap width. All metal structures are treated by a surface impedance model to incorporate ohmic losses.

Like in former simulations [32], the analysis is a two-step procedure: first, the structure is excited at the WR28 waveguide aperture by a modulated Gaussian pulse in the frequency range between 30 and 40 GHz. From the reflected signal at the waveguide port the resonance frequency and the Q_L value are extracted by a special implementation of a Prony-Pisarenko-type method for a highly accurate pole-estimation. In a subsequent simulation run on the same grid model, the electric and magnetic fields at the resonance frequency are monitored by an online discrete Fourier transformation. The total simulation time amounts to 20–30 min. on a standard PC (2×3.0 GHz Pentium CPU).

The resonance detected in the simulations is at $f_0 = 34.52$ GHz with a quality factor $Q_L = 800$, which is in excellent agreement with the measurements of the LGR *B*.1 shown in Tables 1 and 2. Both the resonance frequency and the *Q*-value show a strong sensitivity to geometrical parameters such as the gap width or the diameter of the sample tube. The corresponding frequency shifts can be observed in the simulations as well as in the measurements. The field plots are shown in Fig. 3a–f. They are normalized to an incoming wave of 1 W peak power at the resonance frequency [32]. The empty quartz tube used for the simulations is 0.9×0.7 mm in diameter and has a dielectric constant $\varepsilon_r = 3.8$. Fig. 3a shows a cross-sectional representation of the E_1-field vectors in the *y*–*z* plane. The main field strength is homogenously distributed in the two gaps with opposite phase, the E_1-strength near the 2 mm i.d. outer loop (right) is stronger than near the 1 mm i.d. sample loop (left). Fig. 3b shows the E_1-field intensity in a three-dimensional representation in the *x*–*y* plane at half high (middle) of the resonator. Attention should be given to the four peak values that are close to the sample tube at the sample-hole-to-gap transitions since they indicate a high displacement current density that should not be attenuated or disturbed for optimal resonator performance by i.e. the sample tube or a metallic frequency tuning rode [21]. An E_1-field drop to 10% of the maximum is observed in the center area. Aqueous samples could be placed in a flat cell of dimensions 0.7×0.25 mm in the *x*–*y* plane, see Fig. 3c.

Fig. 3d and e shows the B_1-field strength in contour and vector representation, respectively. With a sample length equal to that of the resonator ($h = 3$ mm) the homogeneity of the B_1-field is 18%, for a sample length of 2.1 mm the homogeneity in the sample is 6%. At the edges, on top, and on the bottom the drops are to 60%. The B_1-field strength homogeneity along the *y*-axis is within 10% of the field maximum and decays gradually along the gap to 10%. Fig. 3f shows the distribution of the B_1-field strength during sample excitation (also expected during the electron spin induction) in a three-dimensional representation.

3. Applications

3.1. CW-EPR

For CW-EPR spectroscopy the resonant structures BLGR and LGR have been predominately used in the frequency range between 1 and 4 GHz. In the pioneering work by Froncisz et al. [21], a *two-loop-one-gap* resonator was also introduced at 35 GHz. Due to the high mw efficiency of this resonant structure, the excitation power applied to obtain a certain B_1-field in the sample is much lower than with conventional rectangular or cylindrical resonant cavities. This fact allows a *S*/*N* improvement by increasing the exciting mw power providing the sample does not saturate. A *S*/*N* improvement of a factor of 3 (from 30 to 90) was achieved with resonator *B*.1 for a Cu(II)(L-histidine monohydrochloride monohydrate) complex by increasing the mw power from 15 to 4000 μW.

3.2. Pulse EPR

The pulse performance of the resonator *B*.3 is demonstrated by a number of experiments which, in particular, require large B_1-fields for optimum sensitivity and resolution.

3.2.1. Double-quantum coherence experiments

The dipole coupling between two (or more) electron spins can be measured by excitation of double-quantum (DQ) electron coherence. Fig. 4a shows a six-pulse DQ coherence sequence which comprises the DQ coherence generator $\pi/2$–τ_1–π–τ_1–$\pi/2$ and the DQ coherence detector $\pi/2$–τ_2–π–τ_2–*echo* [43–45]. In this sequence the delay τ_1 is incremented while τ_2 is decreased with the total time of the whole pulse sequence remaining constant.

The echo is then modulated by the electron–electron coupling, with the unwanted features being removed by phase cycling [43]. Optimum DQ coherence generation requires strong B_1-fields and a large resonator bandwidth,

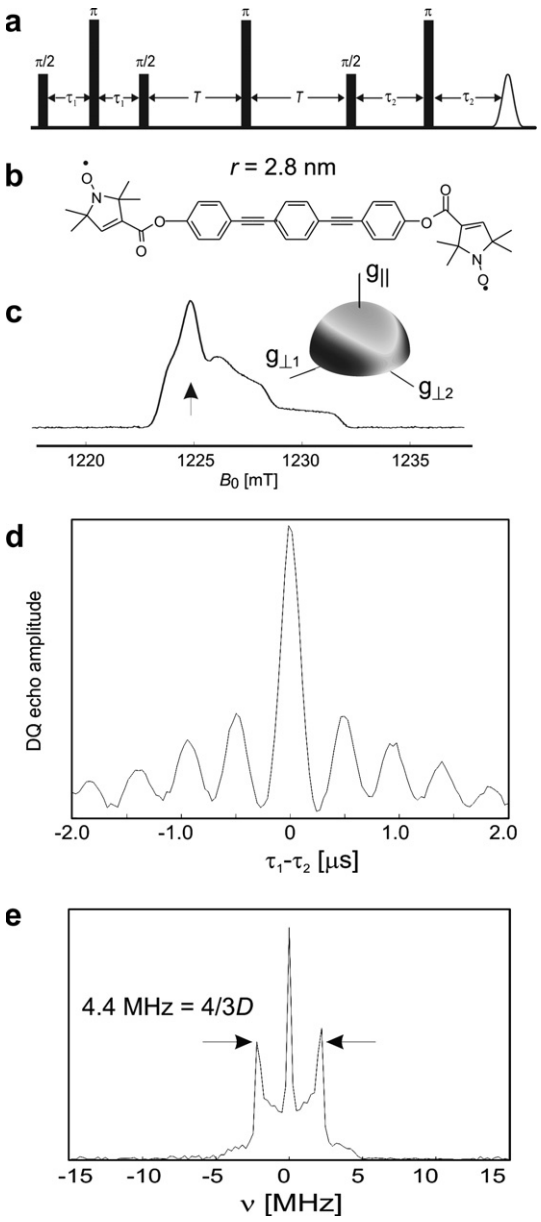

Fig. 4. (a) Six-pulse DQ ESR sequence for measuring electron–electron distances. (b) Biradical with an electron–electron distance of 2.8 nm. (c) Echo-detected EPR spectrum. Arrow shows the position of the DQ ESR experiment, and the orientation selectivity at this field position is depected by the unit sphere (white areas are off resonance with the mw pulses). (d) Time-domain trace of the DQ ESR experiment recorded at 70 K. (e) Fourier transform of (d). The nominal mw pulse lengths were $t_{\pi/2} \sim 4$ ns, $t_{\pi} \sim 4$ ns, $\Delta\tau = 16$ ns, with a 256 step phase cycle, resonator $Q_L \sim 200$–270 (bandwidth 175–130 MHz), mw $\pi/2$ pulse achieved with a power ~15 W ($B_1 \sim 22$ mT). Note the nominal 4 ns pulses consist of an exponential pulse rise (and fall) in ~1 ns with a roof of ~3.5 ns, total time ~5–6 ns. The total measurement time was ca. 30 min. Sample concentration 0.5 mg of biradical/gram of *o*-terphenyl.

making the LGR an ideal structure to implement this technique. The excellent sensitivity of the experiment with the LGR is demonstrated on a biradical with an electron–electron (*e*–*e*) distance of 2.8 nm (Fig. 4b). Fig. 4c shows an echo-detected EPR spectrum from the biradical and the position of the DQ experiment is depicted by the arrow. Fig. 4d and e shows the DQ experimental time-domain trace and its Fourier transform, respectively. With the resonator bandwidth and pulse lengths used in our experiment full spectral excitation is not achieved and thus a complete (powder averaged) Pake pattern is not observed. This can be appreciated by inspection of the orientation selection plot in Fig. 4c, orientations near $g_{\|}$ are not fully excited (black indicates orientations excited by the pulses, white regions are not excited or are off resonance). Nevertheless, the turning points indicated in Fig. 4e which correspond to orientations where $\mathbf{B}_0$ is perpendicular to the interspin *e*–*e* vector allows the *e*–*e* distance to be reliably estimated, $r \sim 2.8$ nm ($D = -7800/r^3$ MHz) [46]. The complete Pake pattern could be obtained by combining this spectrum with an additional measurement along $g_{\|}$, which would also provide limited information on the relative orientation of the EPR interactions of the biradical.

Since at Q-band the spectral spread due to *g*-anisotropy is still relatively small ($g_{\perp 1} = 2.0094$, $g_{\perp 2} = 2.0094$, $g_{\|} = 2.0021$) the spread of the field-swept EPR spectrum is to a large extent still governed by the nitrogen hyperfine interaction ($A_{\perp} = 20$ MHz, $A_{\|} = 94$ MHz), thus the Q-band results are very similar to those obtained at K- and X-band by Borbat et al. [44,45]. At approximately W-band and higher good orientation selection could be achieved.

3.2.2. HYSCORE

HYSCORE [47] is an experiment relying on the creation and detection of nuclear coherence using mw pulses, see sequence in Fig. 5a, to provide information which allows the hyperfine and nuclear quadrupole interactions to be determined. For an $S = 1/2$, $I = 1/2$ spin system excited with ideal mw pulses the maximum modulation amplitude (giving maximum signal intensity) occurs when $|A_s| = 2|\omega_I|$, away from this condition the modulation amplitude decreases rapidly (A_s is the hyperfine coupling and ω_I the nuclear Larmor frequency). When this 'exact cancellation' condition is not met, theory shows that optimum nuclear coherence can be created with matched mw pulses (Fig. 5b), which in the strong coupling case ($|A_s| > 2|\omega_I|$) equates to a strong B_1-field [48,49]. In the HYSCORE sequence the first two mw pulses generate nuclear coherence, and the matched mw pulse has an optimum B_1 strength and length t_m to generate nuclear coherence by exciting the forbidden transitions (Fig. 5b). Usually in the strong coupling case the optimum B_1 can not be reached experimentally, but the LGR implemented here allows mw pulses with very high B_1-fields to be generated and a new region to be investigated experimentally. This is illustrated in Fig. 5c which shows that the pyrrole nitrogens of the nickel porphyrinoid in the enzyme methyl-coenzyme reductase (MCR) [50] can be measured with good sensitive using matched mw pulses, in this case with a strength of $\omega_1/2\pi = 83.3$ MHz ($\omega_1 = g\beta_e B_1/z\hbar$, and $\omega_I/2\pi \sim 3.5$ MHz, $|A_s|/2\pi \sim 30$ MHz). Note that with the typical B_1-field strength obtained with commercially available spectrometers and resonators these pyrrole signals are not

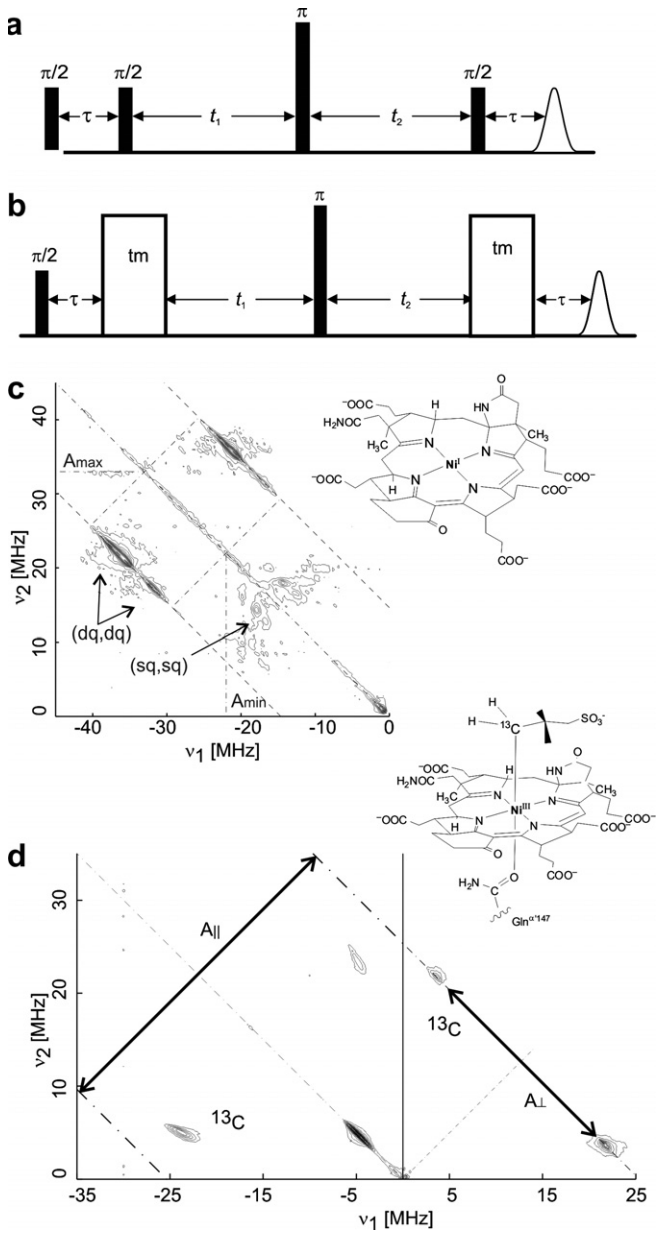

Fig. 5. (a) HYSCORE sequence, and (b) Matched HYSCORE sequence. (c and d) Matched HYSCORE experiments using strong B_1-fields. (c) Enhancement of signals from the strongly coupled nitrogens directly coordinated to the Ni(I) ion of cofactor F_{430}, sample concentration ~1 mM. The mw pulse lengths were $t_{\pi/2} = 6$ ns (41.7 MHz), $t_{\pi,t} = 6$ ns (83.3 MHz), with matched pulses of length $t_m = 42$ ns and strength 83.3 MHz ($t_{10} = t_{20} = 96$ ns, $\Delta t = 12$ ns, data matrix 256×256, and $\tau = 108$ ns). (d) ^{13}C spectrum from the MCR species featuring a nickel alkyl bond (MCR_{BPS}), sample concentration ~1 mM. The mw pulse lengths were $t_{\pi/2} = 12$ ns (20.8 MHz), $t_{\pi,t} = 8$ ns (62.5 MHz), with matched pulses of length $t_m = 12$ ns and strength 62.5 MHz ($t_{10} = t_{20} = 96$ ns, $\Delta t = 12$ ns, data matrix 400×400, and $\tau = 108$ ns).

visible. Fig. 5d gives a second example, again from the enzyme MCR, which features a Ni^{III}-alky bond with the strongly coupled ^{13}C nucleus ($\omega_{13C}/2\pi = 3.5$ MHz) having the hyperfine interaction $|A(^{13}C)| = (18, 18, 46)$ MHz [51]. Again the sensitivity of the experiment was increased using short intense mw pulses.

3.2.3. Hyperfine decoupling

The interpretation of nuclear frequency spectra can be simplified if the hyperfine interaction can be eliminated by decoupling the electron spin(s) with very strong mw B_1-fields [48]. The theoretical analysis of the eigenvalues of the spin Hamiltonian under a strong mw pulse gives for an $S = 1/2$, $I = 1$ spin system [52]

$$\begin{aligned}
\omega^{\mathrm{dec}}_{\mathrm{SQ1}(\alpha,\beta)} &= \omega_{\mathrm{SQ1}} \pm \frac{A\Omega_S}{2\omega_1} \pm \frac{A^2}{4\omega_1} + \frac{B^2}{8(\omega_I \mp \omega_1)} \\
\omega^{\mathrm{dec}}_{\mathrm{SQ2}(\alpha,\beta)} &= \omega_{\mathrm{SQ2}} \pm \frac{A\Omega_S}{2\omega_1} \mp \frac{A^2}{4\omega_1} + \frac{B^2}{8(\omega_I \pm \omega_1)} \\
\omega^{\mathrm{dec}}_{\mathrm{DQ}(\alpha,\beta)} &= \omega_{\mathrm{DQ}} \pm \frac{A\Omega_S}{\omega_1} + \frac{B^2\omega_I}{4(\omega_I^2 - \omega_1^2)},
\end{aligned} \tag{1}$$

where the subscripts SQ1 and SQ2 denote the two single-quantum nuclear spin transitions $(m_I, m_I + 1) = (0, 1)$ and $(-1, 0)$, and DQ the double-quantum nuclear spin transition, $(-1, 1)$. A and B describe the secular and pseudo-secular parts of the hyperfine coupling, respectively [5]. In Eq. (1) the first term on the right hand side gives the desired nuclear frequencies corresponding to complete decoupling ($A = 0$, $B = 0$), whereas the remaining terms describe the residual hyperfine splitting. Clearly a larger ω_1 gives a better decoupling. This is illustrated in Fig. 6, which shows hyperfine-decoupled DEFENCE experiments [53] for the nitrogen of the bis(acetylacetonato) oxovanadium(IV) complex [54] with two different decoupling fields. In Fig. 6c ridges instead of peaks occur along the decoupling dimension because the B_1-field is too weak to completely decouple the hyperfine interaction, in Fig. 6d with $\omega_1/2\pi \sim 120$ MHz the situation is much clearer and the frequencies ω_{DQ} and ω_{SQ1} can be accurately read off the graph. This allows the nuclear quadrupole frequencies to be obtained since the nuclear Zeeman frequency can be directly calculated at the experimental B_0-field.

As for HYSCORE, decoupling experiment requires a large modulation depth for good sensitivity along the ESEEM dimension (ν_1 axis), which depends on the hyperfine and nuclear quadrupole interactions as compared to the nuclear Zeeman frequency (which scales with B_0). In general a multi-frequency approach is thus required with Q-band covering an important range.

3.2.4. High-spin systems

Another advantage of the high mw pulse efficiency Λ_p is that a high power mw amplifier might not be needed for many experiments. Moreover, for certain spin systems even very short mw π pulses can be realized with a low power (100 mW) amplifier. This is the case in the example displayed in Fig. 7. The HYSCORE spectrum of the protein Myoglobin was recorded using the standard sequence shown in Fig. 5a and only a modest 100 mW mw solid-state amplifier. This protein has an electron spin quantum number of $S = 5/2$ and for a given B_1 value the pulses have a higher turning angle as compared to an $S = 1/2$ system [55]. This fact, together with the high Λ_p of the resonator

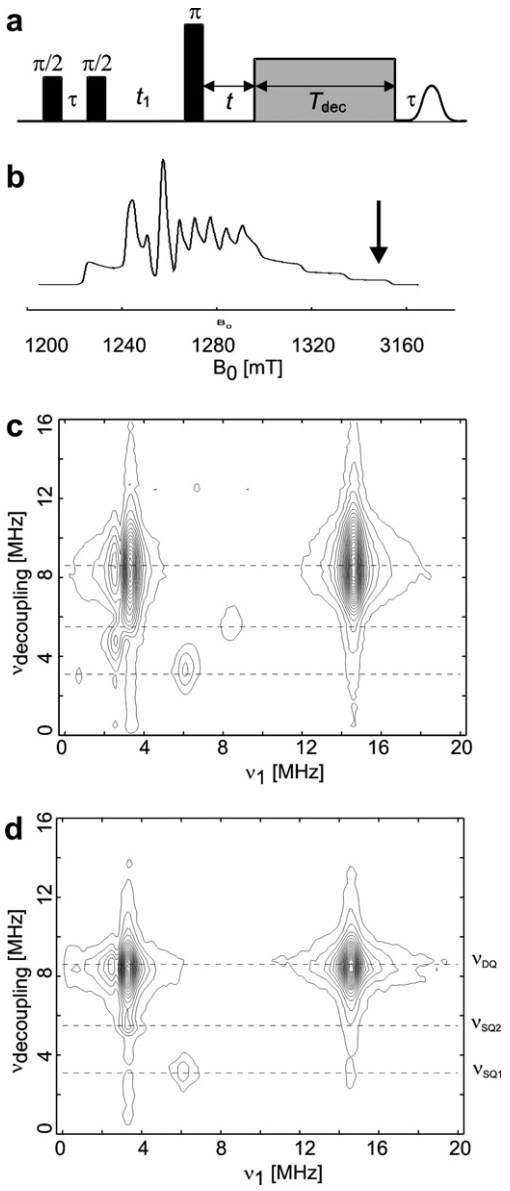

Fig. 6. (a) Hyperfine-decoupled DEFENCE sequence. (b) FID-detected EPR spectrum of bis(acetylacetonato)oxovanadium(IV)/pyridine in a frozen $CHCl_3$/toluene (1:1) solution. Arrow shows the field position of the hyperfine-decoupled DEFENCE experiment for the nitrogen with the B_1-field strength of (c) $\omega_1/2\pi \sim 63$ MHz, and (d) $\omega_1/2\pi \sim 120$ MHz. The experimental parameters were: $\tau = 140$ ns; $t_1 = 170$ ns; starting value for t, $t_0 = 96$ ns incremented in steps of $\Delta t = 16$ ns; starting value for T_{dec}, $T_0 = 16$ ns incremented in steps of $\Delta T_{dec} = 8$ ns (256×512 data points).

allowed $\pi/2$ and π pulses of length 16 ns with a power of only 10 and 40 mW, respectively. Moreover, due to the short relaxation times of the spin system the experiment could be performed at a high repetition rate (6.6 kHz) that is not achievable with our TWT amplifier due to duty cycle limitations.

The spectrum in Fig. 7 was recorded with the static magnetic field close to the perpendicular of the heme plane of the protein. Signals due to the strongly coupled pyrrole nitrogens of the Fe^{3+} heme group are detected in the second quadrant. In the first quadrant signals due to protons,

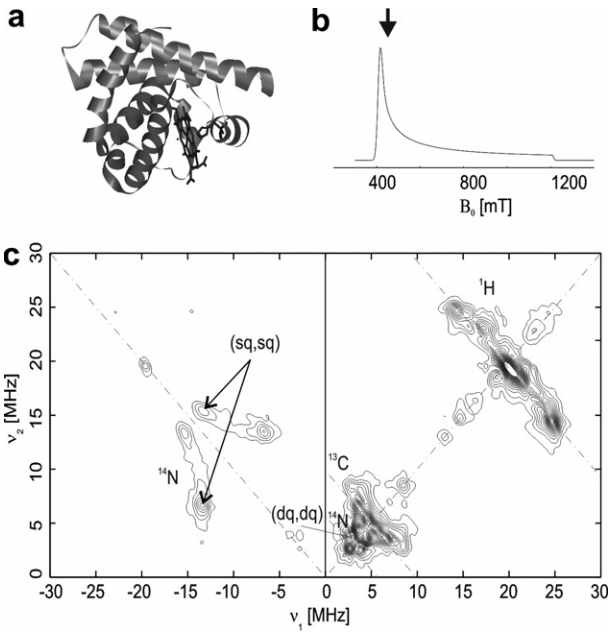

Fig. 7. *HYSCORE* from a metmyoglobin sample measured with LGR *B*.3. (a) Structure of horse heart metmyoglobin showing the active site comprising of a Fe-porphyrin ring coordinated by a histidine residue. The sample was prepared at a concentration of 5 mM with 30% glycerol in a Hepes 100 mM pH 7 buffer. (b) FID-detected EPR spectrum of metmyoglobin, the arrow shows the field position at which the HYSCORE spectrum was recorded. (c) HYSCORE spectrum recorded at a magnetic field of 455 mT and a temperature of 5.5 K. Pulse lengths were: $t_{\pi/2} = t_\pi = 16$ ns, and $\tau = 80$ ns. An eight-step phase cycle was used to eliminate unwanted echoes. The time intervals t_1 and t_2 were varied from 96 to 4000 ns in steps of 16 ns and signal averaging was performed at a repetition rate of 6.6 kHz. The power of the $\pi/2$ and π pulses was 10 and 40 mW, respectively.

remote nitrogens, and carbons (^{13}C in natural abundance 1%) are observed.

4. Conclusion

The use of the LGRs in pulse EPR at 35 GHz provides intense and homogeneous B_1-fields in the sample volume, extending and optimizing the experimental B_1 range with the available excitation power. The LGR is ideally suited to applications requiring large B_1-fields and resonator bandwidths, as was demonstrated with DQ ESR, HYSCORE, and hyperfine decoupling experiments. It fulfills the demand to generate a high S/N ratio for samples in an EPR sample tube (e.g. o.d. = 0.9 mm) that can be directly used at 9.6 GHz (X-band) and 94 GHz (W-band). The ease of construction of a cryogenic probehead for different LGR operating between 34 and 36 GHz and allowing easy sample exchange is outlined.

Acknowledgments

This work was supported by the Swiss National Science Foundation. The authors thank Barbara Feurer for mechanical work and M. Hausammann for his skilled elec-

tro spark work and support for the fabrication process of the LGRs, Peter Müller (Collini Flühman AG) for high quality electroplated LGRs, Gunnar Jeschke for providing the biradical sample, and Arthur Schweiger for all his years of support.

References

[1] I. Gromov, J. Shane, J. Forrer, R. Rakhmatoullin, Y. Rozentzwaig, A. Schweiger, A Q-band pulse EPR/ENDOR spectrometer and the implementation of advanced one- and two-dimensional pulse EPR methodology, J. Magn. Reson. 149 (2) (2001) 196–203.
[2] P. Höfer, R. Heilig, D.C. Maier, I. Prisecaru, D. Schmalbein, The super Q-FT accessory for pulsed EPR, ENDOR and ELDOR at 34 GHz, Bruker Spin Report 152/153 (2003) 37–43.
[3] A.V. Astashkin, J.H. Enemark, A. Raitsimring, 26.5–40 GHz Ka-Band Pulsed EPR Spectrometer, Concepts in Magnetic Resonance Part B, Mag. Res. Eng. 29B (2006) 125–136.
[4] C.E. Davoust, P.E. Doan, B.M. Hoffman, Q-band pulsed electron spin-echo spectrometer and its application to ENDOR and ESEEM, J. Magn. Reson. A 119 (1996) 38–44.
[5] A. Schweiger, G. Jeschke, Principles of Pulse Electron Paramagnetic Resonance, Oxford University Press, Oxford, 2001.
[6] C.P. Poole, Electron Spin Resonance, Wiley, New York, 1967.
[7] C.P. Poole, Electron Spin Resonance, second ed., Dover, New York, 1983.
[8] S. Pfenninger, J. Forrer, A. Schweiger, T. Weiland, Bridged loop gap resonator a resonant structure for pulsed electron-spin-resonance transparent to high-frequency radiation, Rev. Sci. Instrum. 59 (1988) 752–760.
[9] S. Pfenninger, A. Schweiger, J. Forrer, R.R. Ernst, Echo-induced ESR spectroscopy with magnetic field vector jumps: a novel approach to improve the spectral resolution in disordered systems, Chem. Phys. Lett. 154 (1989) 199–204.
[10] Th. Wacker, A. Schweiger, Fourier transform hyperfine spectroscopy, Chem. Phys. Lett. 191 (1992) 136–141.
[11] J. Forrer, S. Pfenninger, G. Sierra, G. Jeschke, A. Schweiger, B. Wagner, Th. Weiland, Probeheads and instrumentation for pulse EPR and ENDOR spectroscopy with chirped radio frequency pulses and magnetic field steps, Appl. Magn. Reson. 10 (1996) 263–279.
[12] M. Willer, J. Granwehr, J. Forrer, A. Schweiger, Two-dimensional nuclear-Zeeman-resolved electron spin echo envelope modulation (NZ-ESEEM) spectroscopy, J. Magn. Reson. 133 (1998) 46–52.
[13] S. Pfenninger, J. Forrer, A. Schweiger, Th. Weiland, Versatile applications of the bridged loop-gap resonator, Phys. Med. 2–4 (1989) 203–212.
[14] C. Gemperle, A. Schweiger, Pulsed electron–nuclear double resonance methodology, Chem. Rev. 91 (1991) 1481–1501.
[15] J. Forrer, S. Pfenninger, A. Schweiger, A pulsed ENDOR probehead with the bridged loop-gap resonator—construction and performance, Rev. Sci. Instrum. 61 (1990) 3360–3367.
[16] J. Forrer, S. Pfenninger, B. Wagner, Th. Weiland, Progress in instrumentation for pulsed EPR and ENDOR spectroscopy, Pure Appl. Chem. 64 (1992) 865–872.
[17] G. Jeschke, A. Schweiger, Time-domain chirp electron nuclear double-resonance spectroscopy in one and two dimensions, J. Chem. Phys. 103 (1995) 8329–8337.
[18] C. Bühlmann, A. Schweiger, R.R. Ernst, Hyperfine-selective ENDOR, Chem. Phys. Lett. 154 (1989) 285–291.
[19] H. Cho, S. Pfenninger, J. Forrer, A. Schweiger, Radio-frequency driven electron-spin-echo envelope modulation spectroscopy, Chem. Phys. Lett. 180 (1991) 198–206.
[20] J. Forrer, Puls ESR spektrometer mit loop-gap-resonator bull, ASE/UCS 75 (1984) 1264.
[21] W. Froncisz, T. Oles, J. Hyde, Q-band loop-gap resonator, Rev. Sci. Instrum. 57 (1986) 1095–1099.
[22] R. Wood, W. Froncisz, J. Hyde, The loop-gap resonator. 2. Controlled return flux 3-loop, 2-gap microwave resonators for ENDOR and electron-spin-resonance spectroscopy, J. Magn. Reson. 58 (1984) 243–253.
[23] S. Pfenninger, W. Froncisz, J. Forrer, J. Luglio, J.S. Hyde, General method for adjusting the quality factor of EPR resonators, Rev. Sci. Instrum. 66 (1995) 4857–4865.
[24] R. Biehl, The dielectric ring TE011 cavity, Bruker Report 1 (1986) 45.
[25] J. Forrer, S. Pfenninger, A. Schweiger, Th. Weiland, Bridged-loop-gap and dielectric resonators for pulsed ESR and ENDOR spectroscopy with light excitationMagnetic Resonance and Related Phenomena, vol. 219, Elsevier, 1989, pp. 919–924.
[26] A.D. Blumlein, High frequency electrical conductor or radiator, US Patent No. 2 238 770 (April 15 1941).
[27] J.S. Hyde, J.-J. Yin, W.K. Subczynski, T.G. Camenisch, J.J. Ratke, W. Froncisz, Spin-label EPR T-1 values using saturation recovery from 2 to 35 GHz, J. Phys. Chem. B 108 (2004) 9524–9529.
[28] R.R. Mett, J.W. Sidabras, J.S. Hyde, Uniform radio frequency fields in loop-gap resonators for EPR spectroscopy, Appl. Magn. Reson. 31 (2007) 573–589.
[29] R. Eichel, A. Schweiger, Polarization-transfer electron-Zeeman resolved EPR, Chem. Phys. Lett. 358 (2002) 271–277.
[30] R. Eichel, A. Schweiger, Right-angle wiggling electron paramagnetic resonance spectroscopy, J. Chem. Phys. 115 (2001) 9126–9135.
[31] J. Granwehr, J. Forrer, A. Schweiger, Longitudinally detected EPR—improved instrumentation and new pulse schemes, J. Magn. Reson. 151 (2001) 78–84.
[32] B. Simovic, P. Studerus, S. Gustavsson, R. Leturcq, K. Ensslin, R. Schuhmann, J. Forrer, A. Schweiger, Design of Q-band loop-gap resonators at frequencies of 34–36 GHz for single electron spin spectroscopy in semiconductor nanostructures, Rev. Sci. Instrum. 77 (2006). Art. No. 064702..
[33] A. Schweiger, L. Braunschweiler, J.M. Fauth, R.R. Ernst, Coherent and incoherent echo spectroscopy with extended-time excitation, Phys. Rev. Lett. 54 (1985) 1241–1244.
[34] J.M. Fauth, A. Schweiger, L. Braunschweiler, J. Forrer, R.R. Ernst, Elimination of unwanted echoes and reduction of dead time in 3-pulse electron spin-echo spectroscopy, J. Magn. Reson. 66 (1986) 74–85.
[35] L. Braunschweiler, Elektronenspinecho-Spektroskopie mit Langzeit-Anregung, Diss. ETH No. 7887.
[36] I. Gromov, J. Forrer, A. Schweiger, Probehead operating at 35 GHz for continuous wave and pulse electron paramagnetic resonance applications, Rev. Sci. Instrum. 77 (2006). Art. No. 064704..
[37] Angst und Pfister, CH-8600, Dübendorf, Switzerland.
[38] Collini-Flühmann AG 8600, Dübendorf, Switzerland.
[39] M. Willer, J. Forrer, J. Keller, S. Van Doorslaer, A. Schweiger, R. Schuhmann, T. Weiland, S-band (2–4 GHz) pulse electron paramagnetic resonance spectrometer: construction, probe head design, and performance, Rev. Sci. Instrum. 71 (2000) 2807–2817.
[40] P. Höfer, P. Carl, X-band pulse–EPR resonator performance, Bruker Report 157/158 (2006) 52–56.
[41] J. Forrer, J. Keller, S. Stoll, G. Jeschke, A. Schweiger, Influence of microwave coupling elements on the electromagnetic field distribution and loaded Q-values of pulse EPR mw resonators, in: M.E. Smith, J.H. Strange (Eds.), Magnetic Resonance and Related Phenomena—Extended book of Abstracts of the 28th Congress Ampere, University of Kent at Canterbury, 1996, pp. 35–36.
[42] CST Microwave Studio: CST GmbH, Darmstadt, Germany, www.cst.com.
[43] S. Saxena, J.H. Freed, Theory of double quantum two-dimensional electron spin resonance with application to distance measurements, J. Chem. Phys. 107 (1997) 1317–1340.
[44] P.P. Borbat, J.H. Freed, Multiple-quantum ESR and distance measurements, Chem. Phys. Lett. 313 (1999) 145–154.
[45] P.P. Borbat, J.H. Freed, Double-quantum ESR and distance measurements, in: L.J. Berliner et al. (Eds.), Biological Magnetic Resonance, vol. 19, Kluwer Academic/Plenum Publishers, New York, 2000, pp. 383–459.

[46] S.S. Eaton, G.R. Eaton, Distance measurements by CW and pulsed EPR, in: L.J. Berliner, S.S. Eaton, G.R. Eaton (Eds.), Biological Magnetic Resonance, vol. 19, Kluwer Academic/Plenum Publishers, New York, 2000, pp. 1–27.

[47] P. Höfer, A. Grupp, H. Nebenführ, M. Mehring, Hyperfine sublevel correlation (HYSCORE) spectroscopy: a 2D ESR investigation of the squaric acid radical, Chem. Phys. Lett. 132 (1986) 279–282.

[48] G. Jeschke, A. Schweiger, Generation and transfer of coherence in electron-nuclear spin systems by non-ideal microwave pulses, Mol. Phys. 88 (1996) 355–383.

[49] G. Jeschke, R. Rakhmatullin, A. Schweiger, Sensitivity enhancement by matched microwave pulses in one- and two-dimensional electron spin echo envelope modulation spectroscopy, J. Magn. Res. 131 (1998) 261–271.

[50] U. Ermler, W. Grabarse, S. Shima, M. Goubeaud, R.K. Thauer, Crystal structure of methyl coenzyme M reductase: the key enzyme of biological methane formation, Science 278 (1997) 1457–1462.

[51] D. Hinderberger, R.R. Piskorski, M. Goenrich, R.K. Thauer, A. Schweiger, J. Harmer, B. Jaun, A nickel-alkyl bond in an inactivated state of the enzyme catalyzing methane formation, Angew. Chem., Int. Ed. Engl. 45 (2006) 3602–3607.

[52] G. Mitrikas, A. Schweiger, Hyperfine decoupling in electron paramagnetic resonance as a powerful tool for unraveling complicated ESEEM spectra of $S = 1/2$, $I \geqslant 1/2$ systems, J. Magn. Reson. 168 (2004) 88–96.

[53] S. Van Doorslaer, A. Schweiger, New hyperfine-decoupling schemes in electron paramagnetic resonance spectroscopy, Chem. Phys. Lett. 308 (1999) 187–194.

[54] B. Kirste, H. van Willigen, Electron nuclear double resonance study of bis(acetylacetonato)oxovanadium(IV) and some of its adducts in frozen solution, J. Chem. Phys. 86 (1982) 2743–2749.

[55] I. García-Rubio, A. Angerhofer, A. Schweiger, EPR and HYSCORE investigation of the electronic structure of the model complex $Mn(imidazole)_6$: exploring Mn(II)-imidazole binding using single crystals, J. Magn. Res. 184 (2007) 130–142.